Electrocatalysis

Deutsche Ausgabe: DOI: 10.1002/ange.201502173
Internationale Ausgabe: DOI: 10.1002/anie.201502173

Iron Carbide Nanoparticles Encapsulated in Mesoporous Fe-N-Doped Carbon Nanofibers for Efficient Electrocatalysis**

*Zhen-Yu Wu, Xing-Xing Xu, Bi-Cheng Hu, Hai-Wei Liang, Yue Lin, Li-Feng Chen, and Shu-Hong Yu**

Abstract: *Exploring low-cost and high-performance nonprecious metal catalysts (NPMCs) for oxygen reduction reaction (ORR) in fuel cells and metal–air batteries is crucial for the commercialization of these energy conversion and storage devices. Here we report a novel NPMC consisting of Fe_3C nanoparticles encapsulated in mesoporous Fe-N-doped carbon nanofibers, which is synthesized by a cost-effective method using carbonaceous nanofibers, pyrrole, and $FeCl_3$ as precursors. The electrocatalyst exhibits outstanding ORR activity (onset potential of −0.02 V and half-wave potential of −0.140 V) closely comparable to the state-of-the-art Pt/C catalyst in alkaline media, and good ORR activity in acidic media, which is among the highest reported activities of NPMCs.*

Oxygen reduction reaction (ORR) is an important process in various energy conversion and storage systems (ECSS) such as fuel cells, metal–air batteries and chloralkali electrolysis.[1] It is critical to develop nonprecious metal catalysts (NPMCs) with high ORR performance to replace Pt-based catalysts for practical applications of these ECSS. In general, the performances of NPMCs are governed by two crucial factors: 1) the intrinsic nature of active sites, which are determined by chemical composition and the interactions between different components; 2) the accessible part of active sites and the transport properties of ORR-relevant species (H^+/OH^-, O_2, H_2O, e^-), which are determined by specific surface area (SSA) and porous structure.[2] Consequently, researchers mainly pay attention to the two aforementioned aspects when designing and preparing various NPMCs.

To achieve catalysts with highly efficient intrinsic active sites, a wide range of different components for NPMCs have been explored, including transition-metal-coordinating macrocyclic compounds,[3] pyrolyzed metal/nitrogen/carbon (M-N_x/C, M = Fe, Co, Ni) compounds,[1c,4] metal oxides and chalcogenides supported on carbon nanotubes or graphene,[5] and metal-free carbon materials doped with heteroatoms.[6] Among the best is the M-N_x/C catalyst, for which the active sites are believed to involve surface nitrogen coordinated with metals.[2a,7] Recently, a new type of highly efficient NPMC, metal/metal carbide nanoparticles encapsulated in nanostructured carbon was developed, whose active sites were believed to be the graphitic carbon shells activated by the encapsulated nanoparticles.[8] On the other hand, many strategies have been developed to create high SSAs and various types of pores with NPMCs expecting to obtain highly active ORR catalysts. The template method, a common but effective route, has been extensively employed to synthesize porous carbon-based NPMCs.[2b,6b,9] In addition, using preexisting porous precursors[8b,10] and postactivation methods[11] are two other effective strategies for preparing high SSA porous NPMCs. Despite tremendous efforts, the desired ORR electrocatalysts, which exhibit the above two features and thus achieve a high performance comparable with Pt/C, have rarely been achieved so far.

Herein, we report a new type of NPMCs based on Fe_3C nanoparticles encapsulated in mesoporous Fe-N-doped carbon nanofibers (hereafter referred to as Fe-N-CNFs), which are synthesized by a cost-effective method using carbonaceous nanofibers, pyrrole, and $FeCl_3$ as precursors. Such a unique catalyst possesses the above desired features for ORR, including multiple highly effective intrinsic active sites (i.e., Fe-N_x/C and Fe_3C@graphitic carbon), high SSA ($425\ m^2 g^{-1}$), and mesoporous structure, as well as a highly graphitic carbon fibrous networks. Consequently, the electrocatalyst shows outstanding ORR activity closely comparable to Pt/C catalyst in alkaline media, and good ORR activity in acidic media.

An illustration for synthesizing Fe-N-CNF electrocatalysts is illustrated in Scheme 1 (for details see the Supporting Information, SI). Prior to the synthesis of catalysts, highly uniform carbonaceous nanofibers with a diameter of ca. 60 nm were prepared on a large scale using a hydrothermal carbonization method based on our previous reports (Figure S1).[12] The obtained carbonaceous nanofibers were first mixed with pyrrole monomers under vigorous stirring (step 1), followed by the dropwise addition of $FeCl_3$ solution to fully polymerize the pyrrole (step 2). After complete polymerization, the mixture was filtered and washed. Then

[*] Z. Y. Wu,[+] X. X. Xu,[+] B. C. Hu, Dr. H. W. Liang, Dr. Y. Lin, Dr. L. F. Chen, Prof. Dr. S. H. Yu
Division of Nanomaterials & Chemistry
Hefei National Laboratory for Physical Sciences at Microscale
Collaborative Innovation Center of Suzhou Nano Science and Technology, Department of Chemistry
University of Science and Technology of China
Hefei, Anhui 230026 (P. R. China)
E-mail: shyu@ustc.edu.cn
Homepage: http://staff.ustc.edu.cn/~yulab/

[+] These authors contributed equally to this work.

[**] This work is supported by the National Natural Science Foundation of China (Grants 21431006, 91227103, 21061160492, J1030412), and the Ministry of Science and Technology of China (Grants 2014CB931800, 2013CB933900), and the Scientific Research Grant of Hefei Science Center of CAS (2015SRG-HSC038).

Supporting information for this article is available on the WWW under http://dx.doi.org/10.1002/anie.201502173.

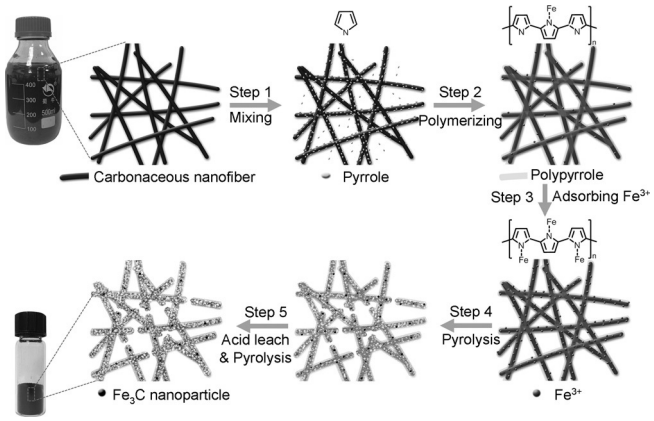

Scheme 1. Synthesis of Fe-N-CNF catalysts.

the as-obtained wet hybrid was dispersed in $FeCl_3$ solution to adsorb Fe^{3+} until saturation (step 3). Subsequently, the Fe^{3+}-saturated hybrid was collected and dried, and then subjected to pyrolysis under N_2 atmosphere (step 4). To remove unstable and ORR-nonreactive phases, the pyrolyzed product was preleached in H_2SO_4 solution. Finally, the preleached catalyst was pyrolyzed for the second time at the same temperature (step 5) to afford the Fe-N-CNF electrocatalyst.

Previous studies showed that the heat-treatment temperature played a crucial role in the performance of pyrolyzed carbon-based NPMCs.[4a,d] Therefore, we first examined the ORR activity of the Fe-N-CNFs catalysts as a function of pyrolysis temperature in the range of 600–1000 °C with rotating disk electrode (RDE) measurements performed in O_2-saturated 0.1 M KOH electrolyte. The highest ORR activity was achieved at 800 °C, which was revealed by the onset and half-wave potentials as well as diffusion-limiting current in linear sweep voltammetry (LSV) curves (Figure S2 a,b and Table S1), probably because a balance of electrical conductivity, porosity, and type and density of active site could be optimized at this temperature.[2b,13] Accordingly, the Fe-N-CNF catalysts discussed below were prepared at 800 °C unless otherwise specified. Further, when keeping the amount of CNFs unchanged, the volume of pyrrole monomer added in carbonaceous nanofibers solution was optimized to be 0.6 mL, as shown by the electrochemical analysis (Figure S2 c,d and Table S2).Thus we chose this volume of pyrrole in our following synthetic procedure. For comparison, carbon nanofibers (CNFs), nitrogen-doped CNFs (N-CNFs), and iron-doped CNFs (Fe-CNFs) were also prepared in a similar way.

Scanning electron microscopy (SEM) and transmission electron microscopy (TEM) observations of Fe-N-CNFs indicated that uniform CNFs with a diameter of ca. 130 nm and several micrometers in length interlinked with each other to form a fibrous network (Figure 1 a–c). The enlarged TEM image showed that the catalyst possessed a unique structure in which the CNFs were porous and some nanoparticles were encapsulated within them (Figure 1 d). Moreover, high-angle annular dark-field scanning TEM (HAADF-STEM) further indicated the nanoparticle-encapsulation structure (Figure 1 e). Remarkably, the products obtained at other pyrolysis

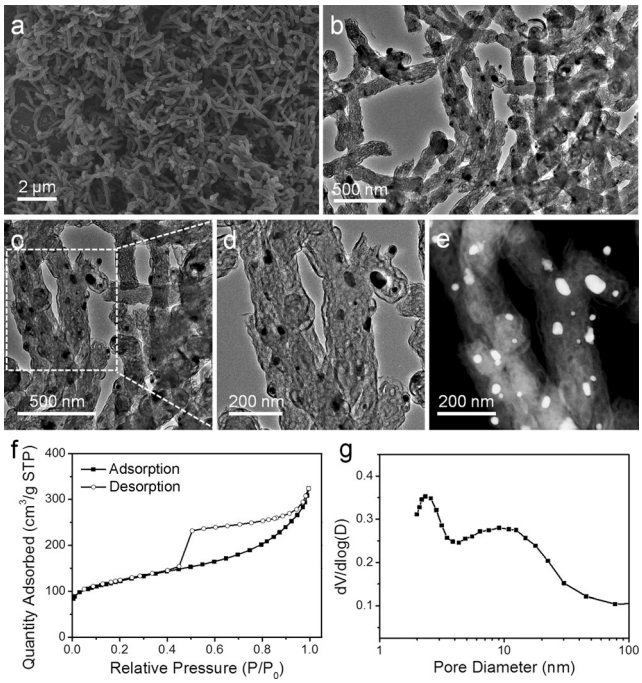

Figure 1. a) SEM image, b–d) TEM images with different magnifications, and e) HAADF-STEM image of Fe-N-CNFs. f) N_2 sorption isotherms and g) pore size distribution of Fe-N-CNFs.

temperatures and different amounts of pyrrole also exhibited a porous structure similar to that of the optimal Fe-N-CNFs except for the sample prepared at 600 °C (Figures S3 and S4), which is probably attributed to the poor graphitization degree at this relatively low temperature. A possible pore formation process for our catalyst system is proposed in the SI (Figures S5 and S6).

The comparative samples (CNFs, N-CNFs, and Fe-CNFs) were also examined by SEM and TEM, and the results are showed in Figure S7. The porous nature of Fe-N-CNFs and three comparative samples was further assessed by N_2 sorption analysis (Figures 1 f,g and S8). The remarkable hysteresis loops of type-IV indicated the mesoporous structure of Fe-N-CNFs and Fe-CNFs, and the mesopore size distribution was centered at 2.3 nm and 10.8 nm for Fe-N-CNFs, and 44.5 nm for Fe-CNFs, respectively. However, the N_2 adsorption curves of CNFs and N-CNFs featured combined characteristics of type I and II, indicating the existence of micropores and macropores, but no obvious pore size distribution was observed in the range of 1–100 nm. The Brunauer–Emmett–Teller surface area and total pore volume of these four samples were 492 $m^2 g^{-1}$ and 0.25 $cm^3 g^{-1}$ (CNFs), 235 $m^2 g^{-1}$ and 0.14 $cm^3 g^{-1}$ (N-CNFs), 447 $m^2 g^{-1}$ and 0.60 $cm^3 g^{-1}$ (Fe-CNFs), and 425 $m^2 g^{-1}$ and 0.44 $cm^3 g^{-1}$ (Fe-N-CNFs), respectively (Table S3). In other words, the Fe-N-CNFs and Fe-CNFs exhibit the desired mesoporous structure with high SSA and large pore volume. Such features are favorable for active site exposure and rapid ORR-relevant species transport.

X-ray photoelectron spectroscopy (XPS) measurements were conducted to elucidate the chemical composition and element bonding configurations in the Fe-N-CNFs. As

expected, the survey spectrum of the catalyst revealed the presence of C (91.28 at %), N (3.78 at %), O (3.88 at %), and Fe (1.05 at %) elements (Figure S9a and Table S4). The complex N 1s spectra could be deconvoluted into three peaks assignable to the pyridinic N (398.7 eV), graphitic N (401.2 eV), and oxidized N (403.8 eV; Figure S9b).[2b,4b] The peaks at a binding energy of 398.7 eV should also include a contribution from nitrogen bound to iron (N-Fe),[2b] because there is only a small difference between binding energies of pyridinic N and N-Fe. All of these N species were reported to play a crucial role in the ORR process except the uncertain contribution of the oxidized N.[4b,14] The high-resolution XPS spectra of Fe revealed that there was a weak pair of doublets for the Fe $2p_{3/2}$ and Fe $2p_{1/2}$ signals at 711.8 eV and 723.4 eV, and at 714.2 eV and 727.4 eV, suggestive of the presence of metallic iron (or its carbide) and oxidized iron species,[4b,15] and the peak at 719.0 eV was a satellite peak[4b] (Figure S9c). The peak at 711.8 eV in the Fe $2p_{3/2}$ XPS spectrum indicates that the Fe is found as Fe ions coordinated to N, that is, Fe-N bonding.[14b] The comparative samples were also investigated by XPS and the results are summarized in Table S4. The subnanoscale energy-filtered TEM (EFTEM) imaging also indicated the presence of C, N, O, and Fe in the Fe-N-CNFs in accord with XPS results (Figure 2a). Notably, except for the nanoparticle sections, all the elements were homogeneously distributed in the Fe-N-CNFs. Importantly, highly uniformly distributed Fe species existed in carbon/nitrogen matrix at the atomic or subnanoscale level, and the Fe and N signals were highly overlaid with each other, probably suggesting that there were Fe species stabilized by N coordination, which is believed to be active Fe-N_x sites.[2b,14a] Indeed, the Fe-N_x sites have been confirmed by advanced electron microscopy, Mössbauer spectroscopy, and X-ray absorption fine-structure measurements in previous reports.[13,16] As for nanoparticle sections, the very strong Fe signals and weak C signals were observed simultaneously, which might possibly indicate that the nanoparticles consisted of iron carbides. Indeed, the X-ray diffraction (XRD) results (Figure S10) confirmed that the nanoparticles in Fe-N-CNFs were Fe_3C species (JCPDS 65-2412). Remarkably, all the nanoparticles were surrounded by the strong C signals, clearly demonstrating that Fe_3C was encapsulated in the carbon shell.

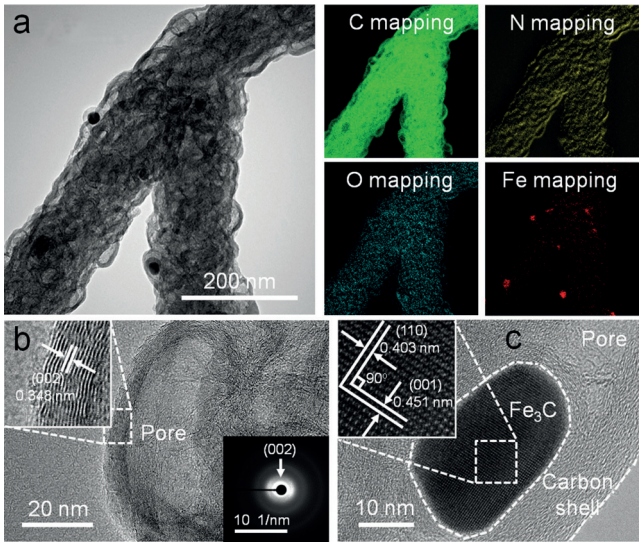

Figure 2. a) EFTEM image and elemental mapping of Fe-N-CNFs. b) HRTEM image of porous sections in Fe-N-CNFs; the top-left inset is an enlarged HRTEM image and the bottom right is the corresponding SAED pattern. c) HRTEM image of nanoparticle sections in Fe-N-CNFs; the top-left inset is an enlarged HRTEM image.

High-resolution TEM (HRTEM) showed the typical mesoporous structure of the nanofibers (Figure 2b). Graphite-like layers could easily be identified at the pore wall with an interlayer spacing of 0.348 nm (the top-left inset of Figure 2b), corresponding to the (002) plane of graphitic carbon. The diffraction ring of (002) plane was also visible in the corresponding selected area electron diffraction (SAED) pattern (the bottom-right inset of Figure 2b). Since it combines the mesoporous graphitic carbon structure with highly active Fe-N_x active sites, the porous sections in Fe-N-CNFs are ideal parts to catalyze ORR. In the nanoparticle sections of Fe-N-CNFs, HRTEM showed the Fe_3C nanoparticle was encapsulated in a highly graphitic carbon shell (Figure 2c). As shown in the inset of Figure 2c for a typical nanoparticle, the spacing of crystalline lattices in two directions was 0.403 nm and 0.451 nm with a characteristic angle of 90°, which matched well with the (110) and (001) planes of Fe_3C phase. The corresponding SAED pattern and high-resolution HAADF-STEM further indicated the crystalline structure of Fe_3C (Figure S11). Based on the above analysis, in the nanoparticle sections of Fe-N-CNFs, crystalline Fe_3C nanoparticles were entirely encapsulated in highly graphitic carbon shell. Previously, density functional calculations and systematic experimental research showed that despite the fact that the encapsulated Fe_3C nanoparticles were not in direct contact with the electrolyte, it could activate the surrounding graphitic layers, making the outer surface of the carbon active toward ORR.[8c,d] Therefore, such a geometric confinement of Fe_3C nanoparticles within graphitic carbon shells has been believed to efficiently improve ORR catalytic activity in our Fe-N-CNFs electrocatalytic system. Possibly, a synergetic catalytic effect may be generated between two active structures (i.e. Fe-N_x and Fe_3C) and thus further enhance the ORR activity.

To evaluate the ORR catalytic activity, cyclic voltammetry (CV) tests were performed on Fe-N-CNFs and three reference CNF-based catalysts as well as a commercial Pt/C catalyst (20% Pt, JM) in 0.1M KOH. In a N_2-saturated electrolyte, the CV curves presented featureless slopes for cathodic current. In sharp contrast, well-defined cathodic peaks were observed for all samples in O_2-saturated electrolyte. Notably, the CV curve in O_2-saturated electrolyte showed that the peak potential at −0.16 V versus the Ag/AgCl electrode afforded by the Fe-N-CNFs catalyst was comparable to that of Pt/C (−0.14 V), but much higher than that of other comparative samples (−0.48, −0.27, and −0.28 V for CNFs, N-CNFs, and Fe-CNFs, respectively; Figures 3a and S12), suggesting a superior ORR catalytic activity for Fe-N-CNFs in alkaline media. The ORR activities of these catalysts were further investigated by LSV polarization curves

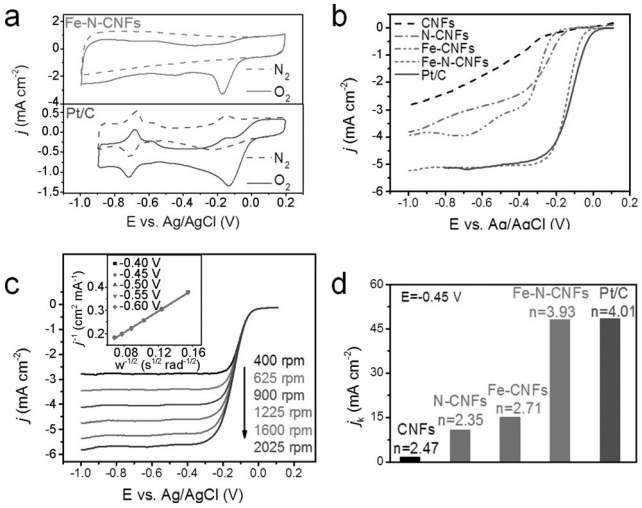

Figure 3. a) CV curves of Fe-N-CNFs and Pt/C. b) LSV curves of all the samples. c) LSVs of Fe-N-CNFs with various rotation rates. The inset in (c) shows the corresponding K-L plots (j^{-1} vs. $\omega^{-1/2}$) at different potentials. d) Kinetic-limiting current density of all the samples at −0.45 V.

(Figure 3b). In accordance with the CV results, the CNFs exhibited worst electrocatalytic activity with a low ORR onset potential of −0.24 V, which is owing to the lack of effective intrinsic active sites for catalyzing ORR. Nitrogen-doping is recognized as one of the most effective strategies to create active sites in carbon materials,[6a,11a] thus the N-CNFs with a high nitrogen content of 9.6 at% showed enhanced ORR activity (onset potential of −0.14 V and half-wave potential of −0.444 V) when compared with pristine CNFs. However, the activity was still not satisfactory for a desired electrocatalyst, probably because low SSAs and poor porous structure of N-CNFs led to a low density of active sites exposed at the electrochemical interface. On the contrary, Fe-CNFs possessed high SSAs, a mesoporous structure, and large pore volume, but was short of effective active sites. Consequently, a mediocre catalytic performance with an onset potential of −0.18 V and a half-wave potential of −0.342 V was observed for Fe-CNFs. Fe-N-CNFs, who combines abundant and highly effective active sites with large SSA and highly mesoporous structure, is considered as an excellent candidate for catalyzing ORR. As expected, Fe-N-CNFs manifested the highest ORR activity among all CNF-based catalysts, and showed an onset potential of −0.02 V and a half-wave potential of −0.140 V, which were closely comparable to that of the commercial Pt/C catalyst (onset potential of 0.01 V and a half-wave potential of −0.120 V; Table S5). To the best of our knowledge, this ORR activity of Fe-N-CNFs is among the highest reported activities of various types of NPMCs (Table S6).

For further insight into the ORR kinetics, the kinetic parameters including electron transfer number (n) and kinetic-limiting current density (j_K) were analyzed on the basis of the RDE tests at various rotating speeds and Koutecky–Levich (K-L) equations. Typically, the current density at the Fe-N-CNFs electrode increased with increasing rotating speeds due to the shortened diffusion distance at high speeds (Figure 3c).[4c] The corresponding K-L plots (j^{-1} vs. $\omega^{-1/2}$) showed fairly good linearity and near coincidence, indicating first-order reaction kinetics toward the concentration of dissolved oxygen and similar electron transfer numbers for ORR at different potentials.[5a] The electron transfer number was calculated to be 3.93–3.95 at the potential ranging from −0.40 to −0.60 V, suggesting that the Fe-N-CNFs hybrid favored a 4e ORR process, similar to ORR catalyzed by a Pt/C catalyst ($n \approx 4.0$, Figure S13g,h). In contrast, the comparative samples showed a much lower electron transfer number of 2.29–2.47 for CNFs, 2.30–2.62 for N-CNFs and 2.63–3.10 for Fe-CNFs, indicating poor electrocatalysis selectivity for these catalysts (Figure S13a–f). Moreover, the kinetic-limiting current density of Fe-N-CNFs was derived from the K-L plots to be 48.15 mA cm^{-2} at −0.45 V, which was much higher than those of Fe-CNFs (15.08 mA cm^{-2}), N-CNFs (10.81 mA cm^{-2}), and CNFs (1.76 mA cm^{-2}), and nearly equal to that of the Pt/C catalyst (48.45 mA cm^{-2}; Figure 3d), further demonstrating synergistic advantages of unique microstructure and desired component for Fe-N-CNFs catalyst. Significantly, the Fe-N-CNFs catalyst showed a better tolerance to the methanol crossover effect and better long-term durability than Pt/C catalyst (Figure S14).

Furthermore, we also evaluated the ORR performance of Fe-N-CNFs in 0.5 M H_2SO_4 electrolyte. A pair of well-developed symmetric peaks was observed for the Fe-N-CNFs electrode in the CV curves, which resulted from the redox reaction between Fe^{II} and Fe^{III} (Figure S15a). The Fe-N-CNFs exhibited a high ORR catalytic activity with an onset potential of 0.55 V versus Ag/AgCl and a half-wave potential of 0.365 V versus Ag/AgCl, whose performance was on the same level as recently reported good results (Figure S15b).[8a,b] The electron transfer number of Fe-N-CNFs was calculated to be 3.70–3.76 at 0 V to −0.20 V, indicating that the Fe-N-CNFs electrode also mainly favored a highly efficient 4e ORR process in acidic media (Figure S15c,d). Up to now, few reports on NPMCs have shown high ORR performance in both alkaline and acidic media. Finally, when used for constructing the air electrode for Zn–air battery, the Fe-N-CNF catalyst exhibited high voltages of 1.30 and 1.21 V at the discharge current densities of 1.0 and 10 mA cm^{-2}, respectively, which are highly comparable with the state-of-the-art Pt/C catalyst (Figure S16). The specific capacity of Fe-N-CNFs-based battery normalized to the mass of consumed Zn was 614 mA h g^{-1} at the discharge density of 10 mA cm^{-2}, corresponding to a high gravimetric energy density of ca. 760 Wh kg^{-1}, which was comparable to that of the Pt/C-based battery (specific capacity of 630 mA h g^{-1}, gravimetric energy density of ca. 790 Wh kg^{-1}). Therefore, the Fe-N-CNF catalyst exhibited a highly comparable performance with the Pt/C catalyst, clearly indicating the great application potential of our developed catalyst (Figure S16).

In summary, we have developed a novel ORR electrocatalyst consisting of Fe_3C nanoparticles encapsulated in mesoporous Fe-N doped carbon nanofibers by a cost-effective method. The catalyst exhibits outstanding ORR activity closely comparable to the Pt/C catalyst in alkaline media, and excellent ORR activity in acidic media, which is among

the highest reported activities of NPMCs. Considering the versatility of metal precursors, our synthesis strategy presented here could be extended to prepare other CNFs-based composites for diverse ECSS, such as lithium-ion batteries, supercapacitors, and water splitting.

Keywords: Fe-N-doped carbon nanofibers · electrocatalysis · iron carbide · mesoporous materials · oxygen reduction reaction

How to cite: *Angew. Chem. Int. Ed.* **2015**, *54*, 8179–8183
Angew. Chem. **2015**, *127*, 8297–8301

[1] a) M. Armand, J. M. Tarascon, *Nature* **2008**, *451*, 652; b) G. Wu, P. Zelenay, *Acc. Chem. Res.* **2013**, *46*, 1878; c) H. T. Chung, J. H. Won, P. Zelenay, *Nat. Commun.* **2013**, *4*, 1922; d) R. Bashyam, P. Zelenay, *Nature* **2006**, *443*, 63.

[2] a) F. Jaouen, E. Proietti, M. Lefevre, R. Chenitz, J.-P. Dodelet, G. Wu, H. T. Chung, C. M. Johnston, P. Zelenay, *Energy Environ. Sci.* **2011**, *4*, 114; b) H.-W. Liang, W. Wei, Z.-S. Wu, X. Feng, K. Müllen, *J. Am. Chem. Soc.* **2013**, *135*, 16002.

[3] a) P.-J. Wei, G.-Q. Yu, Y. Naruta, J.-G. Liu, *Angew. Chem. Int. Ed.* **2014**, *53*, 6659; *Angew. Chem.* **2014**, *126*, 6777; b) R. Cao, R. Thapa, H. Kim, X. Xu, M. Gyu Kim, Q. Li, N. Park, M. Liu, J. Cho, *Nat. Commun.* **2013**, *4*, 2076.

[4] a) H. Peng, Z. Mo, S. Liao, H. Liang, L. Yang, F. Luo, H. Song, Y. Zhong, B. Zhang, *Sci. Rep.* **2013**, *3*, 1765; b) L. Lin, Q. Zhu, A.-W. Xu, *J. Am. Chem. Soc.* **2014**, *136*, 11027; c) J. Liu, X. Sun, P. Song, Y. Zhang, W. Xing, W. Xu, *Adv. Mater.* **2013**, *25*, 6879; d) G. Wu, K. L. More, C. M. Johnston, P. Zelenay, *Science* **2011**, *332*, 443.

[5] a) Y. Liang, Y. Li, H. Wang, J. Zhou, J. Wang, T. Regier, H. Dai, *Nat. Mater.* **2011**, *10*, 780; b) J. Feng, Y. Liang, H. Wang, Y. Li, B. Zhang, J. Zhou, J. Wang, T. Regier, H. Dai, *Nano Res.* **2012**, *5*, 718; c) Y. Liang, Y. Li, H. Wang, H. Dai, *J. Am. Chem. Soc.* **2013**, *135*, 2013; d) H. Wang, Y. Liang, Y. Li, H. Dai, *Angew. Chem. Int. Ed.* **2011**, *50*, 10969; *Angew. Chem.* **2011**, *123*, 11161.

[6] a) K. Gong, F. Du, Z. Xia, M. Durstock, L. Dai, *Science* **2009**, *323*, 760; b) J. Liang, Y. Jiao, M. Jaroniec, S. Z. Qiao, *Angew. Chem. Int. Ed.* **2012**, *51*, 11496; *Angew. Chem.* **2012**, *124*, 11664.

[7] a) Z. Chen, D. Higgins, A. Yu, L. Zhang, J. Zhang, *Energy Environ. Sci.* **2011**, *4*, 3167; b) M. Lefèvre, E. Proietti, F. Jaouen, J.-P. Dodelet, *Science* **2009**, *324*, 71.

[8] a) D. Deng, L. Yu, X. Chen, G. Wang, L. Jin, X. Pan, J. Deng, G. Sun, X. Bao, *Angew. Chem. Int. Ed.* **2013**, *52*, 371; *Angew. Chem.* **2013**, *125*, 389; b) Z.-S. Wu, L. Chen, J. Liu, K. Parvez, H. Liang, J. Shu, H. Sachdev, R. Graf, X. Feng, K. Müllen, *Adv. Mater.* **2014**, *26*, 1450; c) Y. Hu, J. O. Jensen, W. Zhang, L. N. Cleemann, W. Xing, N. J. Bjerrum, Q. Li, *Angew. Chem. Int. Ed.* **2014**, *53*, 3675; *Angew. Chem.* **2014**, *126*, 3749; d) J.-P. Dodelet, R. Chenitz, L. Yang, M. Lefèvre, *ChemCatChem* **2014**, *6*, 1866.

[9] W. Wei, H. Liang, K. Parvez, X. Zhuang, X. Feng, K. Müllen, *Angew. Chem. Int. Ed.* **2014**, *53*, 1570; *Angew. Chem.* **2014**, *126*, 1596.

[10] a) P. Zhang, F. Sun, Z. Xiang, Z. Shen, J. Yun, D. Cao, *Energy Environ. Sci.* **2014**, *7*, 442; b) Z. Xiang, Y. Xue, D. Cao, L. Huang, J.-F. Chen, L. Dai, *Angew. Chem. Int. Ed.* **2014**, *53*, 2433; *Angew. Chem.* **2014**, *126*, 2465; c) Y. Hou, T. Huang, Z. Wen, S. Mao, S. Cui, J. Chen, *Adv. Energy Mater.* **2014**, *4*, DOI: 10.1002/aenm.201400337.

[11] a) H.-W. Liang, X. Zhuang, S. Brüller, X. Feng, K. Müllen, *Nat. Commun.* **2014**, *5*, 4973; b) W. He, C. Jiang, J. Wang, L. Lu, *Angew. Chem. Int. Ed.* **2014**, *53*, 9503; *Angew. Chem.* **2014**, *126*, 9657.

[12] H.-W. Liang, Q.-F. Guan, L.-F. Chen, Z. Zhu, W.-J. Zhang, S.-H. Yu, *Angew. Chem. Int. Ed.* **2012**, *51*, 5101; *Angew. Chem.* **2012**, *124*, 5191.

[13] M. Ferrandon, A. J. Kropf, D. J. Myers, K. Artyushkova, U. Kramm, P. Bogdanoff, G. Wu, C. M. Johnston, P. Zelenay, *J. Phys. Chem. C* **2012**, *116*, 16001.

[14] a) Y. Li, W. Zhou, H. Wang, L. Xie, Y. Liang, F. Wei, J.-C. Idrobo, S. J. Pennycook, H. Dai, *Nat. Nanotechnol.* **2012**, *7*, 394; b) Y. Zhao, K. Watanabe, K. Hashimoto, *J. Am. Chem. Soc.* **2012**, *134*, 19528.

[15] S. Maldonado, K. J. Stevenson, *J. Phys. Chem. B* **2004**, *108*, 11375.

[16] Y. Zhu, B. Zhang, X. Liu, D.-W. Wang, D. S. Su, *Angew. Chem. Int. Ed.* **2014**, *53*, 10673; *Angew. Chem.* **2014**, *126*, 10849.

Received: March 18, 2015
Published online: May 26, 2015

